2006

Cool Flames at Terrestrial, Partial, and Near-Zero Gravity

Michael R. Foster
George Fox University, mfoster@georgefox.edu

Howard Pearlman
Drexel University

Recommended Citation

Cool flames at terrestrial, partial, and near-zero gravity

Michael Foster, Howard Pearlman [*]

Department of Mechanical Engineering and Mechanics, Drexel University, 3141 Chestnut Street, Philadelphia, PA 19104, USA

Abstract

Natural convection plays an important role in all terrestrial, Lunar, and Martian-based, unstirred, static reactor cool flame and low-temperature autoignitions, since the Rayleigh number (Ra) associated with the self-heating of the reaction exceeds the critical Ra (approximately 600) for onset of convection. At near-zero gravity, Ra < 600 can be achieved and the effects of convection suppressed. To systematically vary the Ra without varying the mixture stoichiometry, reactor pressure, or vessel size, cool flames are studied experimentally in a closed, unstirred, static reactor subject to different gravitational accelerations (terrestrial, $1g$; Martian, $0.38g$; Lunar, $0.16g$; a n đ e - duced gravity, $\sim 10^{-2}g$). Representative results show the evolution of the visible light emission using an equimolar n-butane:oxygen premixture at temperatures ranging from 320 to 350 °C (593–623 K) at subatmospheric pressures. For representative reduced-gravity, spherically propagating cool flames, the flame radius based on the peak light intensity is plotted as a function of time and the flame radius (and speed) is calculated from a polynomial fit to data. A skeletal chemical kinetic Gray-Yang model developed previously for a one-dimensional, reactive–diffusive system by Fairlie and co-workers is extended to a two-dimensional axisymmetric, spherical geometry. The coupled species, energy, and momentum equations are solved numerically and the spatio-temporal variations in the temperature profiles are presented. A qualitative comparison is made with the experimental results.

Keywords: Cool flame; Low-temperature reaction; Natural convection; Autoignition; Partial gravity

1. Introduction

Natural convection occurs in a closed reaction vessel when the associated Rayleigh number (Ra) exceeds a critical value (Ra_{cr}) of approximately 600 [1–3]. Typical terrestrial values of the Ra range from 10^4 to 10^6 (or larger) due to the self-heating associated with cool flames and autoignitions and lie in a regime where natural convection and diffusive transport are important. When natural convection occurs, it alters the temperature, hydrodynamic, and species concentration fields [5], resulting in a multidimensional field that is extremely difficult, if not impossible, to be modeled analytically [6]. Kagan and co-workers emphasized this point [4] and further showed that explosion limits may shift depending on the characteristic length scale associated with the flow. Note that at Martian and Lunar gravity, the Ra decreases by roughly three- and sixfold (due to a decrease in g), respectively, which is insufficient to reduce the Ra below the Ra_{cr}.

Moreover, it is recognized that natural convection in unstirred reactors is not "sufficiently strong to generate a spatially uniform temperature distribu-

[*] Corresponding author. Fax: +1 (215) 895 1478.
 E-mail address: hp37@drexel.edu (H. Pearlman).

Nomenclature

Ra	Rayleigh number	Pr	Prandtl number (ν/α)
Ra_{cr}	critical Rayleigh number	$P_{reactants}$	reactant species
g	gravitational acceleration	A	species A (represents a free radical propagating species)
g_z	vertical component of acceleration		
β	coefficient of thermal expansion	a	concentration of species A
ΔT	temperature difference	B	species B (represents a branching species)
ν	kinematic viscosity		
α	thermal diffusivity	b	concentration of species B
R	characteristic length scale	C	products
cc	cubic centimeters	t	time
fps	frames per second	A_n	preexponential factor (n = i, initiation; p, propagation; b, branching; t1, termination step 1; t2, termination step 2)
LLL	low-light level		
uv	ultraviolet		
T	temperature		
T_{wall}	wall temperature	E_n	activation energy (n = i, initiation; p, propagation; b, branching; t1, termination step 1; t2, termination step 2)
$T_{initial}$	initial temperature		
P	pressure		
$P_{initial}$	initial pressure	Q	heat release (exothermicity)
c_p	specific heat at constant pressure	ρ	gas density
D_A	diffusion coefficient of species A	ρ_0	initial gas density
D_B	diffusion coefficient of species B	C_3H_8	propane
Le	Lewis number (α/D)	n-C_4H_{10}	normal butane
		O_2	oxygen

tion throughout the reacting gas" [6]. Thus, an unstirred, nonisothermal reaction does not reduce to that generated in a mechanically, well-stirred system and complications associated with natural convection are therefore unavoidable under terrestrial, Martian, and Lunar conditions.

Historically, the complexities associated with natural convection were recognized as early as 1939 [7] when the thermal ignition theory was first developed. In the 1955 text, *Diffusion and Heat Exchange in Chemical Kinetics*, Frank-Kamenetskii states, "purely conductive theory can be applied at sufficiently low pressure and small dimensions of the vessel when the influence of natural convection can be disregarded." This was reiterated by Tyler in 1966 [1] and further emphasized by Barnard and Harwood in 1974 who stated that "it is generally assumed that heat losses are purely conductive. While this may be valid for certain low pressure slow combustion regimes, it is unlikely to be true for the cool flame and ignition regimes" [3].

To vary the Ra without varying the mixture properties, reaction vessel size, reactor pressure, or mixture stoichiometry, experiments are conducted aboard NASA's KC-135 aircraft, which simulates different effective gravitational accelerations. Intensified video imaging and pressure measurements are made to discern the extent of reaction and the spatio-temporal structure of the reaction. Clearly, natural convection plays a decreasing role with decreasing gravitational level, i.e., decreasing Ra, and diffusive fluxes govern transport.

2. Experimental apparatus

A static, unstirred, spherical, fused-silica reaction vessel is housed in a box furnace. The internal diameter of the vessel is 10.2 cm. The vessel has a fused-silica extension tube for gas feed, exhaust, and vacuum connections. The extension tube penetrates the furnace wall through a ceramic sleeve and connects to a prefilled 50 cc gas cylinder via a solenoid valve. The gas cylinder is charged with an equimolar n-butane:oxygen premixture, which is rapidly injected into the preheated, preevacuated vessel at the start of each test.

The pressure in the reaction vessel is recorded using a Setra Model 204 0–172.4 kPa transducer (accuracy: ± 0.186 kPa) mounted at the entrance to the reactor on the cold side of the furnace. The visible light emission from the reaction is recorded through a side window using a Hamamatsu Model C5909 low-light level video camera and operated ungated at 30 fps at maximum gain. For the radius and velocity profiles reported in Fig. 4, a more sensitive low-light level camera (Dalsa/SMD ICCD-1M30P equipped with a fiber optically coupled 18-mm Gen II UV image in-

tensifier manufactured by Video Scope International, Ltd.) is positioned on the top of the furnace and used to record the light emission.

In all static reactor experiments, the initial conditions must be established within a fraction of the first induction period to ensure that the experimental results are not obscured by residual gas motion and the temperature and pressure have equilibrated. A brief discussion of the times required to achieve thermal equilibration, pressure equilibration, and quiescence follows. For a detailed review of static reactor testing and limitations, refer to the work of Barnard and Harwood [3].

2.1. Thermal equilibration

The time required for thermal equilibration is determined by injecting propane–nitrogen mixtures into a preheated, evacuated vessel while monitoring the temperature in the vessel. Fig. 1a is a plot showing the center temperature for four different prescribed pressures under terrestrial conditions measured with a 0.127 mm diameter type K thermocouple with a response time approximately equal to 0.1 s. Prior to gas injection, the thermocouple is heated radiatively from the preheated vessel and furnace. The cooler gas reduces the thermocouple temperature during gas entry. The temperature then increases exponentially due to conductive heating. The ratio of the change in temperature $\Delta T = (T - T_{wall})$ to the initial temperature excess $\Delta T_0 = (T_0 - T_{wall})$ as a function of time is plotted in Fig. 1b. The average time constant, τ_{avg}, obtained from a curve fit of the form $\exp(-t/\tau)$ is
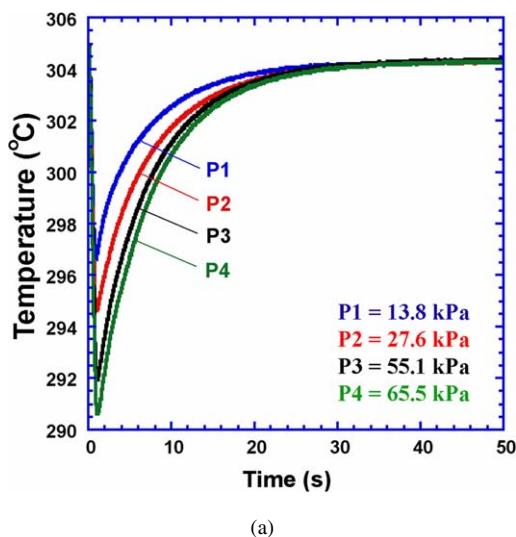
6.5 s, showing little, if any, dependence on the initial pressure.

2.2. Pressure equilibration

The time for pressure equilibration depends on the pressure differential between the cold reactants and the hot vessel, the size of the vessel, the diameter and length of the interconnecting tubing, the valve sizes, and the gas flow path (e.g., pressure drops in tubing and at bends). While there are several contributing factors, the measured time for pressure equilibration ranges from 6 to 8 s, while the induction periods are roughly twice as long (or longer) for the cases reported herein. Thus, pressure equilibration is achieved in about half of the time (or less) of the induction period.

2.3. Quiescence

The hydrodynamic field must also be quiescent within a small fraction of the induction period. The viscous dissipation time ($t_{viscous}$) scales with the square of the vessel radius divided by the kinematic viscosity. For equimolar propane–oxygen at 20 kPa and 600 K, $\nu = 1.4 \times 10^{-4}$ m²/s; thus, $t_{viscous} \sim R^2/\nu = 12.7$ s, roughly half of the measured induction periods.

3. Experimental results

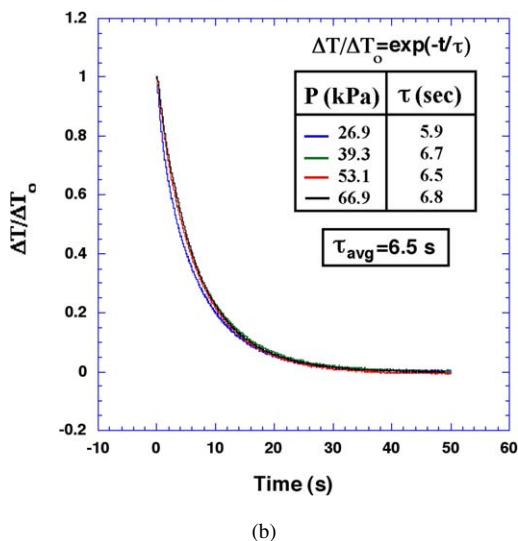The slow heat release that occurs during the induction period is expected to induce a toroidal convective

(a)

(b)

Fig. 1. (a) Temperature history showing preheat times for C_3H_8:N_2 (1.1:1) premixtures ($P_{1-4} = 26.9$, 39.3, 53.1, and 66.9 kPa; $T_{wall} = 305\,°C$); (b) the time constant associated with preheating for different initial pressures ($P_{1-4} = 13.8$, 27.6, 55.1, and 65.5 kPa) at $T_{wall} = 305\,°C$.
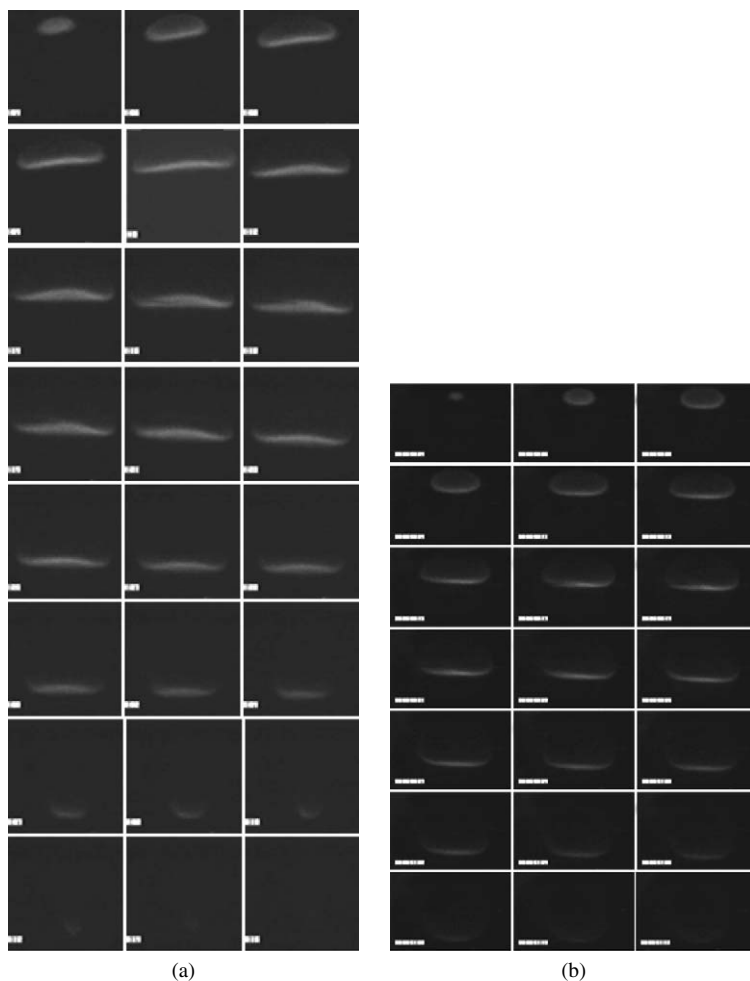
Fig. 2. Intensified side-view cool flame images using an equimolar n-C_4H_{10}:O_2 premixture in a 10.2 cm i.d. vessel at (a) $1g$, (b) $0.38g$, (c) $0.18g$, and (d) $\sim 5 \times 10^{-2}g$ (reduced gravity). In all cases, $T_{wall} = 300\,^{\circ}C$, $P_{initial} = 20.7$ kPa. Time between frames is $1/15$ s (left to right in sequential rows).

flow in the closed vessel for $Ra > 600$ ($1g$, $0.38g$, and $0.18g$ cases) as the hot, less dense gas rises in the bulk and recirculates downward along the internal vessel wall as it cools [8]. Furthermore, the rise speed of the hot gas is expected to scale as $\sqrt{gR}$ and thus decrease as the effective gravitational acceleration (g) decreases. Relative to the terrestrial case, the manifestation of the increasingly weaker convective flows at $0.38g$ and $0.18g$ on the flame is observed indirectly through the observed changes in the flame shape, light emission, and pressure histories. To date, however, this toroidal flow field has not been quantified experimentally.

Fig. 2 shows a sequence of images of a cool flame in an equimolar n-butane:oxygen premixture at different g levels: (a) $1g$, (b) $0.38g$, (c) $0.18g$, and (d) $5 \times 10^{-2}g$, respectively, under otherwise nearly identical test conditions. Note that the airplane can sim-

ulate $0.38g$, $0.18g$, and near-zero gravity for 35, 30, and 20–23 s, respectively.

At $1g$ (Fig. 2a), the cool flame is observed to start near the top of the reactor after a brief induction period of 10 s and proceeds to propagate downward into the reactor. The leading edge of the flame radially expands and curves downward near the reactor walls and upward in the central region. As the flame approaches the base of the reactor, its radius decreases and the extent of inflexion diminishes. Eventually, the flame develops into a single cusp curved toward the base of the vessel. The cusp sharpens; the visible intensity weakens, presumably due to heat and possibly radical species loss; and the flame retreats upward in the direction of the presumed gas flow along the centerline of the reactor. When multiple cool flames occur, the sequence of events repeats and the downward propagation speed relative to the laboratory coordi-
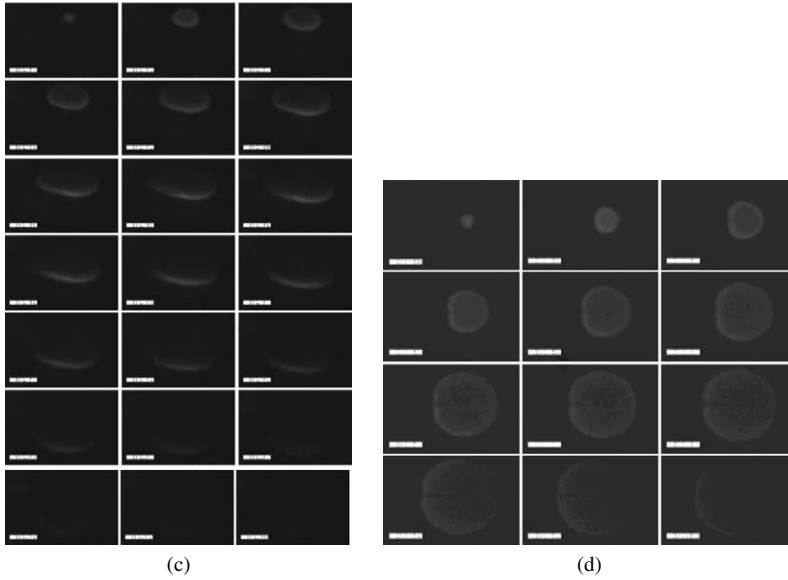
(c)

(d)

Fig. 2. (*continued*)

nate slows with each sequential cool flame. Recognizably, the mixture concentration and temperature fields are transient and spatially nonuniform. Eventually, the reaction slows, the pressure and temperature equilibrate, and no observable light is detected. It is noted that the sensitivity of the camera is insufficient to image the light emission with narrow-band spectral filtering; thus, the integrated ultraviolet and visible emission is reported.

A representative sequence of images is shown in Fig. 2b for experiments conducted at $0.38g$. Similar to $1g$ tests, the flame starts near the top of the reactor and the leading edge propagates downward. No inflexion is observed. As the flame propagates through the reactor, the intensity of the light emission occurring in the trailing region (behind the front) decreases. As the leading edge approaches the base of the reactor, its intensity also decreases. The convective flow speed at $0.38g$ is expected to be about 60% slower than the $1g$ case based on the $g^{1/2}$ scaling.

At $0.18g$ (Fig. 2c), the flame front also starts near the top and propagates downward into the reactor with a more pronounced curvature at the leading edge. This is expected as the induced convective flow speed decreases, coincident with a decrease in gravity.

Fig. 2d shows the reaction at near-zero gravity ($\approx 5 \times 10^{-2}g$); the cool flame starts near the center and propagates spherically outward. The intensity of the internal spectral emission decreases with increasing radius. As the leading edge approaches the reactor wall, the intensity further decreases.

Corresponding pressure histories together with the vertical component of acceleration are plotted in Figs. 3a–3d. The reduced-gravity, Lunar-gravity, and terrestrial tests have similar pressure histories and increasing induction periods, while the Martian-gravity test has the shortest induction period and the broadest pressure peak.

From representative equimolar propane:oxygen cool flame images at reduced gravity, line profiles are tabulated using a commercially available data analysis software package, i.e., IgorPro 5.02. Using a criterium of 60% of the peak signal intensity relative to the background noise level, the flame diameter is determined. A third order polynomial fit is then applied to the data and differentiated to obtain the flame propagation speed. At $T = 320\,^\circ\text{C}$ and pressures between 68.3 and 71.0 kPa, two-stage ignitions are observed at reduced gravity. A comparative plot of radius versus time for the cool flame stage of the reaction at 68.3 kPa (solid line) and 71.0 kPa (dashed line) is shown in Fig. 4a. The flame speed appears slightly faster at 68.3 kPa than at 71.0 kPa, yet the data are within the uncertainty of the measurement. In Fig. 4b, the flame radii and flame speed are plotted as functions of time. The rate of deceleration slows as the flame propagates radially outward and then increases again as the flame approaches the wall. Qualitatively, this result agrees with the numerical prediction for propane cool flames at zero gravity [10].

4. A two-dimensional five-step Gray-Yang model

A one-dimensional five-step, skeletal Gray-Yang model that includes diffusion of species and heat [9] has been extended to two-dimensions to include the effects of natural convection. The model is summa-
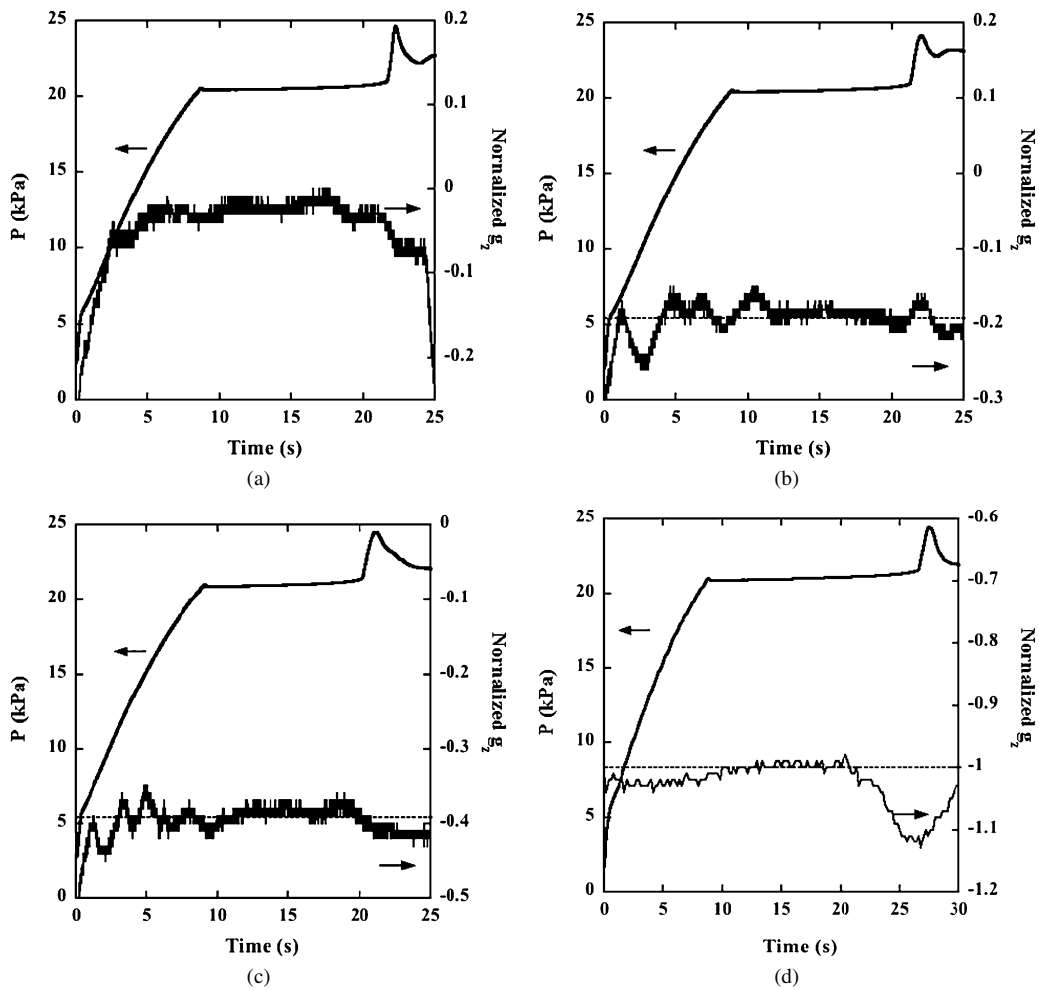
Fig. 3. Pressure histories associated with an equimolar n-C_4H_{10}:O_2 premixture in a 10.2 cm i.d. vessel at (a) near-zero, (b) Lunar, (c) Martian, and (d) terrestrial gravity corresponding with Figs. 1a–1d.
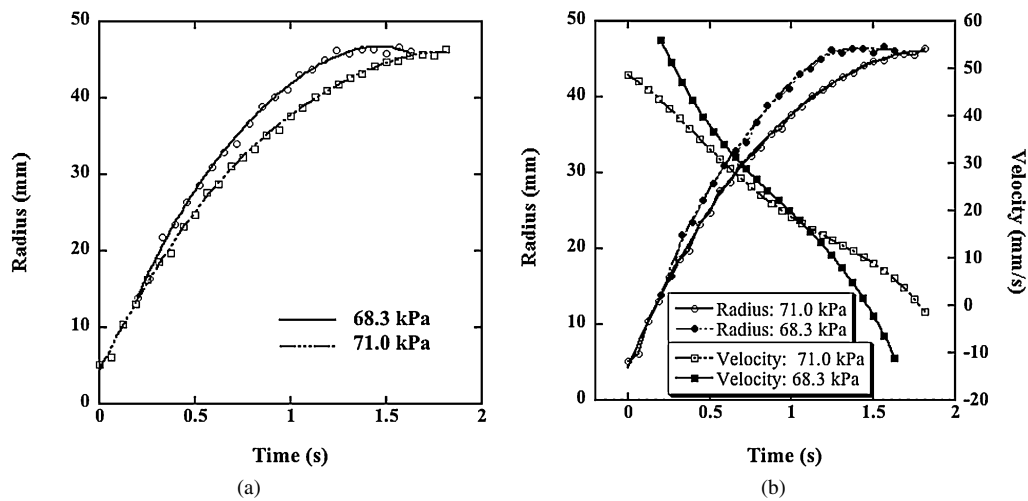

Fig. 4. Cool flame radii (a) and flame speed (b) versus time for equimolar propane:oxygen cool flames at reduced gravity for an initial pressure of 68.3 and 71.0 kPa at 320 °C.

Table 1
The skeletal Gray-Yang five-step modified mechanism adopted from [9]

Five-step modified Gray-Yang reaction mechanism		A_n, preexponential factor (s^{-1})	E_n, activation energy (kJ mol^{-1})	Q, exothermicity (J mol^{-1})
Initiation (k_i)	$P_{\text{reactants}} \rightarrow A$	$A_i = 10^{-6}$	$E_i = 0$	0
Propagation (k_p)	$A \rightarrow B$	$A_p = 10^{6}$	$E_p = 0$	0
Term. 1 (k_{t1})	$A \rightarrow C$	$A_p = 10^{11}$	$E_p = 75$	0
Branching (k_b)	$B \rightarrow 2A$	$A_b = 10^{3}$	$E_b = 45$	10^5
Term. 2 (k_{t2})	$B \rightarrow C$	$A_{t2} = 0.60$	$E_{t2} = 0$	0

rized in Table 1. The boundary conditions are constant wall temperature, inert boundary conditions (no flux), and no-slip velocity at the wall. The initial conditions are spatially uniform gas temperature equal to the fixed wall temperature (T_{wall}), no initial gas velocity, and constant properties ($c_p = 8.6 \times 10^{-4}$ J/cm^3 K; $D_A = D_B = \alpha = \nu = 3$ cm^2/s, Le = Pr = 1) as in Ref. [9]. The Arrhenius reaction rate for each step is of the form $k_n = A_n \exp(-E_n/RT)$.

The conservation equations are as follows.

Species A:

$$\frac{\partial a}{\partial t} + \bar{u} \cdot \nabla a = D_A \nabla^2 a + k_i p_0 \exp(-k_i t) - (k_p + k_{t1})a + 2k_b b.$$

Species B:

$$\frac{\partial b}{\partial t} + \bar{u} \cdot \nabla b = D_B \nabla^2 b + k_p a - k_b b - k_{t2} b.$$

Momentum:

$$\frac{\partial \bar{u}}{\partial t} + \bar{u} \cdot \nabla \bar{u} = -\frac{1}{\rho_0} \nabla p + \nu \nabla^2 \bar{u} + \left(\frac{\rho}{\rho_0}\right) \bar{g}.$$

Energy:

$$\left(\frac{c_v}{c_p}\right)\frac{\partial T}{\partial t} + \bar{u} \cdot \nabla T = \alpha \nabla^2 T + \left(\frac{Qk_b}{\rho_0 c_p}\right)b.$$

The coupled species, momentum, and energy equations are solved using COMSOL Multiphysics, a finite element analysis algorithm for coupled partial differential equations, in a spherically symmetric, two-dimensional half domain using 1416 triangular elements (162 boundary elements, 791 nodes).

The spatio-temporal temperature distribution, the concentration profiles of species A and B, and the associated velocity field are shown in Figs. 5a–5d for gravitational accelerations representative of terrestrial, Martian, Lunar, and zero gravity: (a) $1g$, (b) $0.38g$, (c) $0.16g$, and (d) $0g$. In these computations, the initial wall temperature is fixed at 630 K and the initial pressure is 40 kPa.

Qualitatively, the temperature contours parallel that of the visible emission seen in Figs. 2a–2d. Specifically, a region of high temperature develops near the top of the vessel at $1g$, which subsequently radiates downward into the bulk mixture. At 14.4–14.6 s, colder gas is entrained into the higher temperature region and a toroidal temperature distribution is established with the highest gas temperature near the wall and along the centerline (15.0–16.8 s). The corresponding A and B species concentration distributions are shown at the same time steps and are observed to increase initially near the top of the vessel (13.4–13.6 s) and then rapidly decrease as they are consumed in the high-temperature regions. The peak concentrations eventually develop in the colder regions along the lower wall of the vessel. The corresponding velocity field is also shown. Starting from a quiescent flow, the development of an upward flow along the symmetry axis together with a recirculating flow that moves downward along the vessel walls is observed in qualitative agreement with the results obtained by Cardoso et al. [8]. In essence, the less dense gas rises until it encounters the upper vessel boundary and recirculates downward along the wall to satisfy mass continuity. Note also that the velocity along the centerline and corresponding speed of the recirculating flow are time dependent and oscillatory. Fig. 6 shows the velocity at the center of the vessel as a function of time in the order of decreasing gravitational acceleration: (a) $1g$, (b) $0.38g$, and (c) $0.16g$. Note that the magnitude of the velocity at the center damps as a function of time and decreases with decreasing gravitational acceleration. The buoyantly driven recirculating flow weakens as the gravitational acceleration decreases.

In Figs. 5b and 5c, the temperature and species concentration distributions are increasingly radially symmetric as the gravitational acceleration is decreased. Similar to the $1g$ results, the concentrations of A and B at $0.38g$ and $0.16g$ increase initially in the upper half of the vessel as the temperature increases and are subsequently consumed as the temperature further increases. Eventually, species A and B are in highest concentrations near the vessel walls in the lower temperature regions.

At $0g$ (Fig. 5d), the temperature and species concentrations are radially symmetric. Initially, the temperature increases in the center and then radiates out-
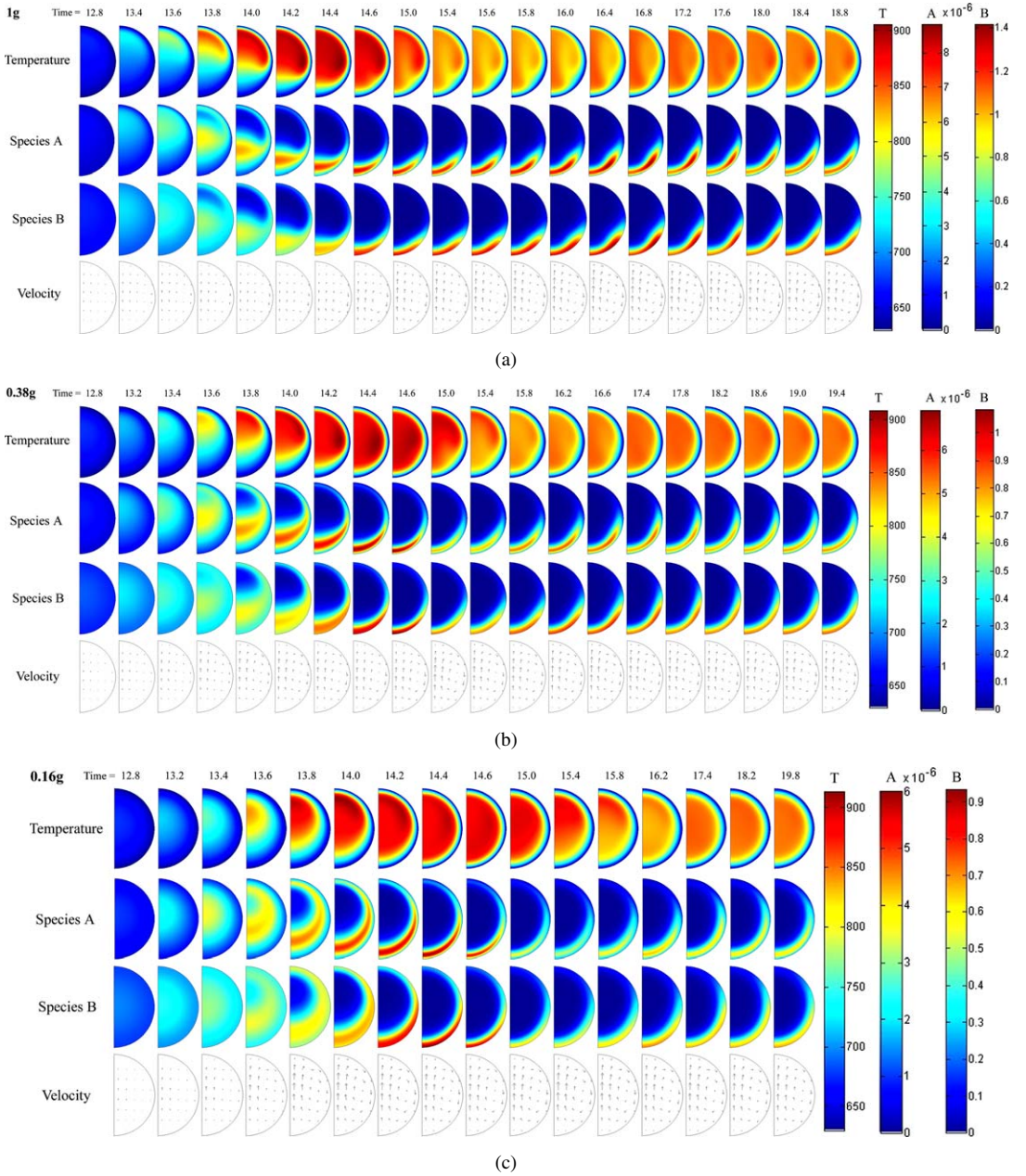
Fig. 5. Predicted time-dependent temperature, A and B species concentration distributions, and velocity fields predicted using the modified Gray-Yang skeletal kinetic model at different gravitational levels at (a) $1g$, (b) $0.38g$, (c) $0.16g$, and (d) $0g$. Temperature scale in K; $T_{wall} = T_{initial} = 630$ K, $P_{initial} = 40$ kPa, $t = 0$–30 s; 1 s of movie = 6 s computational time or 1 s of computational time is 5 frames. Time sequence is from left to right. Color bars in (b)–(d) are the same as shown in (a) for the temperature, A and B species concentrations.

wardly as the concentrations of species A and B increase initially in the center ($t < 13.8$ s) and are consumed as the temperature further increases ($t \geqslant 13.8$ s). Similar to the nonzero gravity results, the highest concentrations of A and B occur in the lower temperature boundary regions.
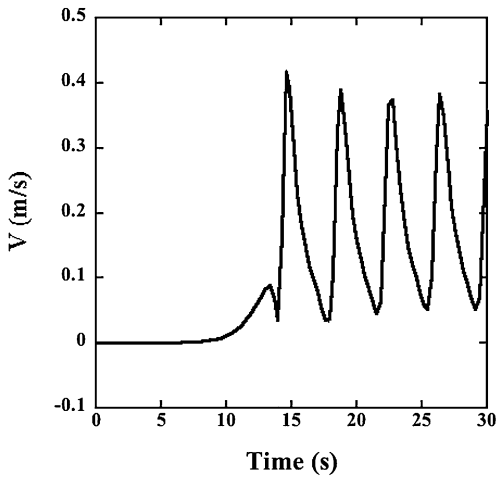
5. Conclusions

The structure and oscillatory behavior of cool flames are strongly affected by natural convection at Earth and partial gravity. As a result, the temperature and species concentration profiles are mod-
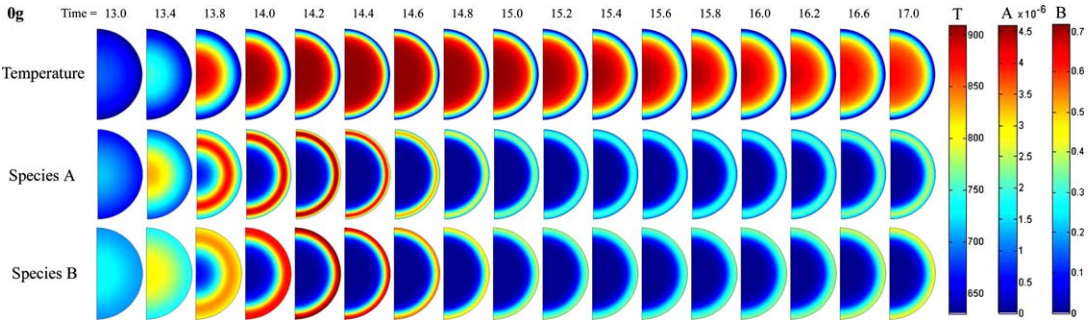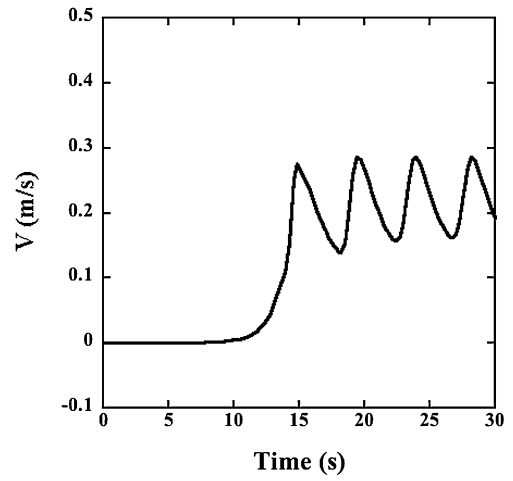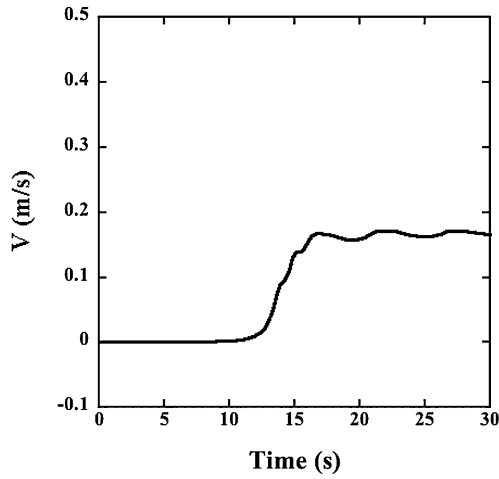
(d)

Fig. 5. (*continued*)

(a)

(b)

(c)

Fig. 6. Predicted vertical component of the velocity at the center of the reactor as a function of time for different gravitational accelerations: (a) 1*g*, (2) 0.38*g*, and (c) 0.18*g*.

ified as suggested by the visible emission records obtained experimentally at different gravitational levels aboard NASA's KC-135 reduced-gravity aircraft together with numerical predictions obtained using a skeletal Gray-Yang two-dimensional model that includes natural convection and diffusive transport of heat and species. In contrast, cool flames at near-zero gravity are observed to be radially symmetric as shown in experiments and model predictions.

Acknowledgment

References

[1] B. Tyler, Combust. Flame 10 (1966) 90–91.

[2] D. Fine, P. Gray, R. MacKinven, Proc. R. Soc. London A 316 (1970) 223–240.

[3] J.A. Barnard, B.A. Harwood, Combust. Flame 22 (1974) 35–42.

[4] H. Kagan, L. Beresycki, G. Joulin, G. Sivashinsky, Combust. Theory Modelling 1 (1997) 97–111.

[5] V. Volpert, C. Barillon, T. Dumont, S. Genieys, M. Massot, in: The Fire and Explosion Conference, Univ. of Central Lancashire, Windermere, UK, August 2000.

[6] J.F. Griffiths, P. Gray, K. Kishore, Combust. Flame 22 (1974) 197–207.

[7] D.A. Frank-Kamenetskii, Zh. Fiz. Khim. 13 (1939) 738.

[8] S. Cardoso, P. Kan, K. Savjani, A. Hayhurst, J. Griffiths, Phys. Chem. Chem. Phys. 6 (8) (2004) 1687–1696.

[9] R. Fairlie, J.F. Griffiths, H. Pearlman, Proc. Combust. Inst. 28 (2000) 1693–1699.

[10] R. Fairlie, J. Griffiths, K. Hughes, H. Pearlman, Proc. Combust. Inst. 30 (2005) 1057–1064.